Harmonically matched grating-based full-field quantitative high-resolution phase microscope for observing dynamics of transparent biological samples

Jigang Wu*, Zahid Yaqoob, Xin Heng, Xiquan Cui, and Changhuei Yang

Department of Electrical Engineering, California Institute of Technology, Pasadena, California, 91125
**Email: jigang@caltech.edu*

Abstract: We have developed a full-field high resolution quantitative phase imaging technique for observing dynamics of transparent biological samples. By using a harmonically matched diffraction grating pair (600 and 1200 lines/mm), we were able to obtain non-trivial phase difference (other than 0^o or 180^o) between the output ports of the gratings. Improving upon our previous design, our current system mitigates astigmatism artifacts and is capable of high resolution imaging. This system also employs an improved phase extraction algorithm. The system has a lateral resolution of 1.6 μm and a phase sensitivity of 62 mrad. We employed the system to acquire high resolution phase images of onion skin cells and a phase movie of amoeba proteus in motion.

OCIS codes: (120.5050) Phase measurement; (050.1950) Diffraction gratings; (170.3880) Medical and biological imaging

References and links

1. F. Zernike, "Phase contrast, a new method for the microscopic observation of transparent objects," Physica **9**, 686-698 (1942).
2. F. Zernike, "Phase contrast, a new method for the microscopic observation of transparent objects Part II," Physica **9**, 974-986 (1942).
3. R. D. Allen, G. B. David, and G. Nomarski, "The Zeiss-Nomarski differential interference equipment for transmitted light microscopy," Z. wiss. Mikr. **69**, 193-221 (1969).
4. K. Creath, "Phase-measurement interferometry techniques," Prog. Opt. **26**, 349-393 (1988).
5. K. J. Chalut, W. J. Brown, and A. Wax, "Quantitative phase microscopy with asynchronous digital holography," Opt. Lett. **15**, 3047-3052 (2007).
6. W. Choi, C. Fang-Yen, K. Badizadegan, S. Oh, N. Lue, R. R. Dasari, and M. S. Feld, "Tomographic phase microscopy," Nature methods **4**, 717-719 (2007).
7. P. Marquet, B. Rappaz, P. J. Magistretti, E. Cuche, Y. Emery, T. Colomb, and C. Depeursinge, "Digital holographic microscopy: a noninvasive contrast imaging technique allowing quantitative visualization of living cells with subwavelength axial accuracy," Opt. Lett. **30**, 468-470 (2005).
8. B. Rappaz, P. Marquet, E. Cuche, Y. Emery, C. Depeursinge, and P. J. Magistretti, "Measurement of the integral refractive index and dynamic cell morphometry of living cells with digital holographic microscopy," Opt. Express **13**, 9361-9373 (2005).
9. J. Kuhn, T. Colomb, F. Montfort, F. Charriere, Y. Emery, E. Cuche, P. Marquet, and C. Depeursinge, "Real-time dual-wavelength digital holographic microscopy with a single hologram acquisition," Opt. Express **15**, 7231-7242 (2007).
10. T. Ikeda, G. Popescu, R. R. Dasari, and M. S. Feld, "Hilbert phase microscopy for investigating fast dynamics in transparent systems," Opt. Lett. **30,** 1165-1167 (2005).
11. G. Popescu, T. Ikeda, K. Goda, C. A. Best-Popescu, M. Laposata, S. Manley, R. R. Dasari, K. Badizadegan, and M. S. Feld, "Optical measurement of cell membrane tension," Phys. Rev. Lett. **97**, 218101 (2006).
12. M. V. Sarunic, S. Weinberg, and J. A. Izatt, "Full-field swept-source phase microscopy," Opt. Lett. **31**, 1462-1464 (2006).
13. D. O. Hogenboom, C. A. DiMarzio, T. J. Gaudette, A. J. Devaney, and S. C. Lindberg, "Three-dimensional images generated by quadrature interferometry," Opt. Lett. **23**, 783-785 (1998).

#87235 - $15.00 USD Received 6 Sep 2007; revised 4 Dec 2007; accepted 14 Dec 2007; published 19 Dec 2007

14. J. Wu, Z. Yaqoob, X. Heng, L. M. Lee, X. Cui, and C. Yang, "Full field phase imaging using a harmonically matched diffraction grating pair based homodyne quadrature interferometer," Appl. Phys. Lett. **90**, 151123 (2007).
15. Z. Yaqoob, J. Wu, X. Cui, X. Heng, and C. Yang, "Harmonically-related diffraction gratings-based interferometer for quadrature phase measurements," Opt. Express **14**, 8127-8137 (2006).
16. M. A. Choma, C. Yang, and J. A. Izatt, "Instantaneous quadrature low-coherence interferometry with 3x3 fiber-optic couplers," Opt. Lett. **28**, 2162-2164 (2003).
17. Z. Yaqoob, J. Fingler, X. Heng, and C. Yang, "Homodyne *en face* optical coherence tomography," Opt. Lett. **31**, 1815-1817 (2006)
18. M. Pilu, A. W. Fitzgibbon, and R. B. Fisher, "Ellipse-specific direct least-square fitting," in *Proceedings of IEEE International Conference on Image Processing* (Lausanne, 1998), vol. **3**, pp. 599-602.
19. D. G. Ghiglia and M. D. Pritt, *Two-Dimensional Phase Unwrapping: Theory, Algorithms, and Software* (John Wiley & Sons, 1998), Section 4.5.
20. C. Yang, "Molecular Contrast Optical Coherence Tomography: A Review," Photochemistry and Photobiology **81**, 215-237 (2005)

1. Introduction

Observing unstained transparent biological samples with sufficiently high resolution is important for a wide range of biomedical studies. Besides conventional qualitative techniques such as Zernike phase contrast [1,2] and Nomarski differential interference contrast (DIC) microscopy [3], various full-field quantitative phase imaging techniques [4-13] have been developed recently that are well suited for this purpose. Most of these methods involve the use of interferometry in one form or another. Some of the prominent techniques are: 1) Phase shifting interferometry schemes [4-6] – where two or more interferograms with different phase shifts are acquired sequentially and a phase image is generated from them. 2) Digital holography [7-9] or Hilbert phase microscopy [10, 11] – where high frequency spatial fringes encoded in the interferogram are demodulated to generate the phase image. 3) Swept-source phase microscopy [12] – where modulation in the interferogram generated by a wavelength sweep can be processed to create a phase image. 4) Polarization quadrature microscopy [13] – where phase images are generated by a polarization based quadrature interferometer.

Recently, our group demonstrated a full-field phase imaging technique based on the substitution of a beamsplitter with a harmonically matched diffraction grating pair (G1G2 grating) [14, 15] in an interferometer – we named the technique G1G2 interferometry. With this optical element substitution, we were able to create a non-trivial phase relationship between the different output ports of the interferometer. Conceptually, the operating principle shares many similarities to the multiport fiber coupler based interferometry method [16, 17]. As G1G2 interferometry involves a minimal change of optical elements – replacement of a beamsplitter, it can be potentially adapted into a wide range of interferometer systems. Phase imaging based on this technique involves simultaneously acquiring images from two or more of the output ports; the imaging speed of this technique is limited only by the cameras' speed. This is an advantage over phase shifting interferometry methods, where the imaging speed is additionally limited by the speed of the phase shifting process. Another appealing aspect of this technique is that data processing is relatively simple. Yet another advantage of this technique is that, unlike some of the other phase techniques, its phase imaging capability does not require a tradeoff in field of view (see discussion in Ref. 5). Specifically, methods such as digital holography and Hilbert phase microscopy perform phase measurements by implementing a spatial sinusoidal interference – each resolvable point on the image is limited by the interference fringe and is by necessity several sensor pixels wide. In comparison, each resolvable point in G1G2 interferometry imaging can be as small as a single sensor pixel.

Our previous implementation of the G1G2 interferometer has a couple of design issues that limit this technique when it is applied for high resolution imaging. Specifically, there were significant aberrations in the raw data image from the output ports when high resolution (1.6 μm) and moderate field of view (400 μm × 300 μm) were required. As a consequence, the coincidence mapping of raw data images is difficult beyond a certain resolution limit. Second, the phase computation algorithm previously employed required either the reference

#87235 - $15.00 USD Received 6 Sep 2007; revised 4 Dec 2007; accepted 14 Dec 2007; published 19 Dec 2007

or sample beam to be much weaker than the other. This limitation can significantly impact on the achievable dynamic range.

This paper reports on our recent progress. We have addressed the two abovementioned design issues and have developed a more robust G1G2 interferometer system. Using this system, we were able to acquire our first high resolution phase images of biological samples based on the G1G2 interferometry principle. The rest of this paper is structured as follows. In Section 2, we summarize the concept of G1G2 interferometry. In Section 3, we present our current experimental setup and discuss the means by which we reduced aberrations. In Section 4, we present our modified phase extraction algorithm that can accommodate the usage of reference and sample beams of comparable strength in the interferometer. In Section 5, we show phase images and videos acquired with our system – this illustrates the capability of the G1G2 interferometer method for biological studies. Finally, we summarize our work in Section 6.

2. G1G2 interferometery concept

This section briefly summarizes the G1G2 interferometry concept. Interested readers are invited to read Ref. 14 and 15 for more in depth explanations.

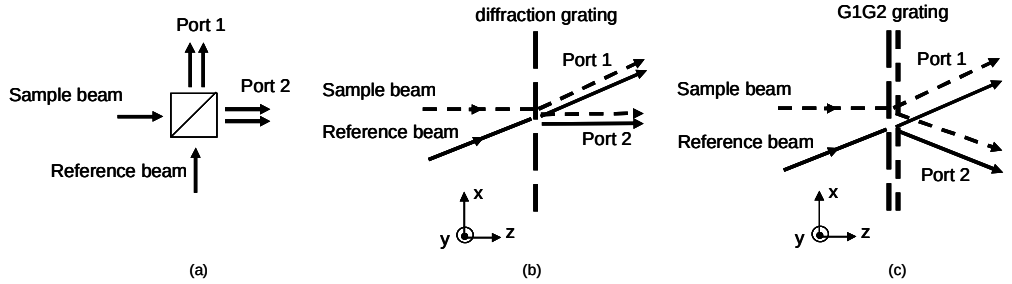

Fig. 1. (a). Simple beamsplitter based interferometer: 180° phase shift between output ports; (b) Single shallow grating based interferometer: still 180° phase shift between output ports; (c) G1G2 grating based interferometer: non-trivial phase shift can be obtained.

First, let us consider a simple interferometer, such as the one shown in Fig. 1(a). The detected signals at the output ports can be expressed as:

$$\text{Port 1: } P_1 = P_r/2 + P_s/2 + \sqrt{P_r P_s}\cos(\psi_s - \psi_r + \theta) \quad (1)$$

$$\text{Port 2: } P_2 = P_r/2 + P_s/2 - \sqrt{P_r P_s}\cos(\psi_s - \psi_r + \theta) \quad (2)$$

where P_r and P_s are the reference power and sample power, respectively; ψ_r and ψ_s are the phase of the reference beam and sample beam before incident on the beamsplitter; θ is the common phase shift. We note that the interference terms are 180° out of phase with each other. As such, it is generally impossible to extract phase information from this system without resorting to some form of phase encoding. An often cited reason to explain this trivial interference phase relationship is that the power influx and outflux from this optical system must be conserved – conservation requires the interference terms to be equal and opposite.

However, power conservation does not intrinsically limit the interference terms to be trivially related. Multiport optical fiber coupler based interferometry methods [16, 17] clearly illustrate that the existence of multiple output ports allows non-trivial interference phase relationship to exist between output ports without violating power conservation. These methods indicate the possibility of using diffraction gratings in place of beamsplitters as a means for achieving non-trivial interference phase relationship in a full-field interferometer, as a diffraction grating can diffract light in more than two directions.

Now let us consider the shallow diffraction grating based interferometer scheme in Fig. 1(b). As is well known, a grating can confer additional phase shifts to the diffracted beams. For a shallow grating, the phase shifts can be written as [15]

#87235 - $15.00 USD Received 6 Sep 2007; revised 4 Dec 2007; accepted 14 Dec 2007; published 19 Dec 2007

$$\phi(x_0) = |m|[\mathrm{sgn}(m)\frac{2\pi x_0}{\Lambda} + \frac{\pi}{2}] \tag{3}$$

where m is the diffracted order, x_0 is the displacement of the grating and Λ is the grating period; sgn() is the sign function. This implies that the detected signals are given by:

$$\text{Port 1: } P_1 = P_{r1} + P_{s1} + 2\sqrt{P_{r1}P_{s1}}\cos(\frac{2\pi x_0}{\Lambda} + \frac{\pi}{2} + \theta) \tag{4}$$

$$\text{Port 2: } P_2 = P_{r2} + P_{s2} + 2\sqrt{P_{r2}P_{s2}}\cos(\frac{2\pi x_0}{\Lambda} - \frac{\pi}{2} + \theta) \tag{5}$$

where P_{r1} (P_{s1}) and P_{r2} (P_{s2}) are the reference (sample) powers at port 1 and port 2, respectively; θ is the common phase shift. The phase relationship between the interference terms remains trivial. However, the presence of a phase shift term $\frac{2\pi x_0}{\Lambda}$ that is intrinsically related to the diffraction grating is encouraging. As we shall soon see, the G1G2 interferometer makes creative use of this phase shift term to achieve non-trivial phase relationship between interferometer output ports.

The G1G2 interferometer replaces the simple diffraction grating in the previous example with a harmonically matched grating pair (G1G2 grating). The grating pair consists of two gratings with periods Λ_1, Λ_2 that satisfy $\Lambda_1=2\Lambda_2$. If the G1G2 grating is used as a beam splitter/combiner in an interferometer setup, as shown in Fig. 1(c), the additional phase of the diffracted beams $\phi_{k,n}$ (k=R, S represent the reference or sample beam; n=1, 2 is the port number) can be written as, according to Eq. (3),

$$\begin{aligned} &\phi_{R,1} = \phi_{0,G1G2} = 0,\ \phi_{S,1} = \phi_{+1,G1} = \frac{2\pi x_1}{\Lambda_1} + \frac{\pi}{2}, \\ &\phi_{R,2} = \phi_{-1,G2} = -\frac{2\pi x_2}{\Lambda_2} + \frac{\pi}{2},\ \phi_{S,2} = \phi_{-1,G1} = -\frac{2\pi x_1}{\Lambda_1} + \frac{\pi}{2} \end{aligned} \tag{6}$$

where $\phi_{m,Gn}$ is the additional phase shift of the m^{th} diffracted order of the grating Gn; x_1, x_2 are the displacements of G1, G2, respectively. Thus the phases of interference signals and their difference are

$$\Delta\phi_1 = \phi_{S,1} - \phi_{R,1} = \frac{2\pi x_1}{\Lambda_1} + \frac{\pi}{2}, \quad \Delta\phi_2 = \phi_{S,2} - \phi_{R,2} = -\frac{2\pi x_1}{\Lambda_1} + \frac{2\pi x_2}{\Lambda_2} \tag{7}$$

$$\Delta\phi = \Delta\phi_2 - \Delta\phi_1 = \frac{4\pi(x_2 - x_1)}{\Lambda_1} - \frac{\pi}{2} \tag{8}$$

As long as $\frac{4\pi(x_2 - x_1)}{\Lambda_1} \neq \left(n + \frac{1}{2}\right)\pi; n \in \mathbf{Z}$, we will have a non-trivial phase shift between the output ports of the interferometer. By adjusting the relative displacement between G1 and G2 grating during fabrication, we can set the phase shift $\Delta\phi$. The grating pair employed in our current experiment was fabricated by using three-beam interference on a holographic plate as detailed in Ref. [14].

3. Experiment method

Our improved experimental setup is shown in Fig. 2. A HeNe laser (Thorlabs HRP120, wavelength of 632.8 nm) was split into reference beam and sample beam. In the reference arm, the laser was spatial filtered and expanded by objective 1 (Newport M-10X), a pinhole (diameter of 25μm) and lens 1 (focal length of 200 mm). The transmitted and diffracted reference beams were then collimated by lens 3 and 4, respectively. The focal lengths of

#87235 - $15.00 USD Received 6 Sep 2007; revised 4 Dec 2007; accepted 14 Dec 2007; published 19 Dec 2007

lenses 2, 3, 4 were all equal to 200 mm. In the sample arm, objective 2 (Olympus UPlanFl 10X) and lens 3 (lens 4) made up the microscope system that imaged the sample onto the CCDs (The Imaging Source DMK 31BF03, 1024x768 pixels). The harmonically matched grating pair (G1G2 grating) served as the beam splitter/combiner. The G1G2 grating pair contains gratings of density 600 lines/mm and 1200 lines/mm. We measured $\Delta\phi$ to be equal to $92^{o}\pm8^{o}$. More details about the grating pair can be found in Ref. 14.

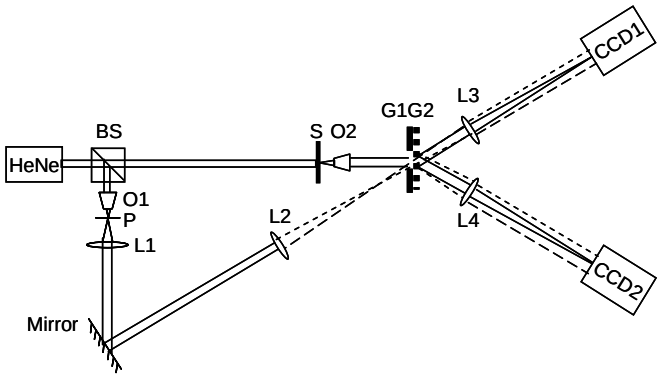

Fig. 2. Experimental setup for phase imaging. BS: beam splitter; O1 and O2: objective lenses 1 and 2; P: pinhole; L1-4: lens 1-4; S: sample; G1G2: the harmonically matched grating pair (G1G2 grating) on a holographic plate.

In this system, the geometric aberration introduced by the grating pair in the previous system was corrected. The imaging system in previous setup [14] is shown in Fig. 3(a); in that setup, the imaging lenses were placed before the grating. The inherent distortion that such geometry introduced can be appreciated by considering the following example. Suppose we are to image a point source using the scheme in Fig. 3(a). We can see that the beam will converge prior to transmission through the grating. As the angle of diffraction associated with the grating does not linearly depend on the incident angle, we can expect to observe geometric aberration in the image. To determine the extent of distortion, we used ZEMAX (ZEMAX development corp.) to simulate this scenario. In the simulation, we assumed the objective and the lens were perfect paraxial lens so that the aberration observed could be solely attributed to the diffraction grating. As shown in Fig. 3(b), when we increase the distance between the imaging plane and the lens, we can observe the image transit from a vertical focus (left) to a horizontal focus (right). This phenomenon is similar to astigmatism. Figure 3(e) shows the transmission image of a letter "C" pattern acquired using the system shown in Fig. 3(a), where the location of the imaging plane was selected to give us vertical focus. The blur in the horizontal direction is readily observable.

To correct this astigmatic aberration, we employed the imaging setup shown in Fig. 3(c), where the grating was put between the objective and the lens. In this case, the incident light associated with each point on the object plane was transformed into a collimated beam at the grating. The collimated beams would diffract from the grating as collimated beams. These would then transform back to point objects in the image plane by passage through the lens. Our Zemax simulations confirmed this fact [see Fig. 3(d)]. Figure 3(f) shows the image of the same letter "C" acquired using this setup, with which we can easily see that the obvious astigmatism aberration had been removed.

We experimentally determined the resolution of this imaging system to be equal to 1.6 μm (Sparrow's criterion) by measuring the image profile of an effective point source (a hole of diameter 150 nm). The measured resolution agreed well with the theoretically calculated value of 1.2 μm based on the imaging system parameters.

This updated setup confers aberrations onto the input collimated light that is used to illuminate the sample [see Fig. 3(g)]. This is because the collimated light will be focused by the objective and will diverge when it enters the grating. The aberration of background beam

#87235 - $15.00 USD Received 6 Sep 2007; revised 4 Dec 2007; accepted 14 Dec 2007; published 19 Dec 2007

will introduce unwanted pattern in the interferograms and unwanted phase aberration in the final phase image. Fortunately, we can measure and characterize this phase aberration during initial system calibration by removing the sample. This systematic error can then be removed from actual sample image measurements during data processing.

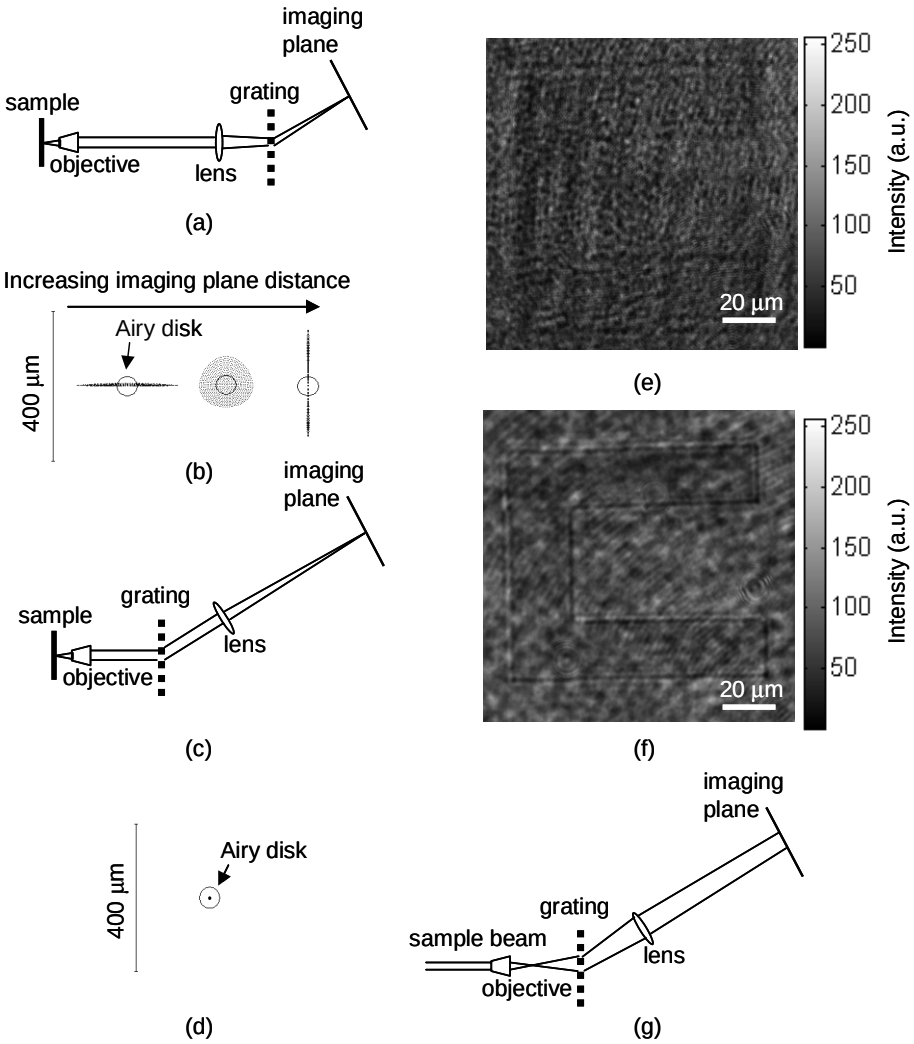

Fig. 3. Geometric aberration induced by the grating. (a) Previous imaging setup; (b) Astigmatism of the focal spots of previous setup; (c) Current imaging setup; (d) No aberration in the focal spot of current setup; (e) Image of letter "C" acquired by the previous setup; (f) Image of letter "C" acquired by the current setup; (g) Aberration of illumination beam caused by the grating diffraction in current setup.

One final aberration issue that we need to be concerned about is the spatial "stretch" and "compression" distortion on the off-axis diffracted raw data image due to the diffraction process. As shown in Fig. 4, the image will be stretched in one direction and compressed in the other direction, and this effect is opposite for +1 and -1 order diffraction of the grating. This distortion in principle will affect the matching of the two CCD images. However, the following calculation shows that the effect is small enough and can be neglected. The distortion is due to the fact that the angle of diffraction associated with the grating does not linearly depend on the incident angle. Mathematically, a point that is x_1 away from the center

#87235 - $15.00 USD Received 6 Sep 2007; revised 4 Dec 2007; accepted 14 Dec 2007; published 19 Dec 2007

of object field will be mapped to a point x_2 from the image field's center where x_2 is given by this expression:

$$x_2 = f_2 \tan\left[\sin^{-1}\left(\frac{\lambda}{d} - \sin(\tan^{-1}\frac{x_1}{f_1})\right) - \sin^{-1}\frac{\lambda}{d}\right] \tag{9}$$

where f_1, f_2 are the focal length of the objective and the lens, respectively; λ is the wavelength of the laser; d is the grating period. Here we assume that both the objective and the lens are perfect paraxial lens. As x_2 is not linearly dependent on x_1, the resulting image will appear distorted. When x_1 is small, Eq. (9) can be simplified as

$$x_2 = \frac{-f_2 / f_1}{\sqrt{1-\lambda^2/d^2}} x_1 \tag{10}$$

where x_2 is proportional to x_1 and there is no distortion. In our setup, f_1=16.5 mm, f_2=200 mm, λ = 632.8 nm, d = 1/600 mm. For the field of view with a maximum offset, x_1 = 0.16 mm, the difference between the two x_2 calculated by (9) and (10) is 4.5 μm, which is smaller than the size of a pixel on the CCDs (pixel size = 4.7 μm). Beyond this field of view, the distortion does cause a slight deterioration in resolution. This problem can be resolved by appropriate spatial rescaling of the raw data images.

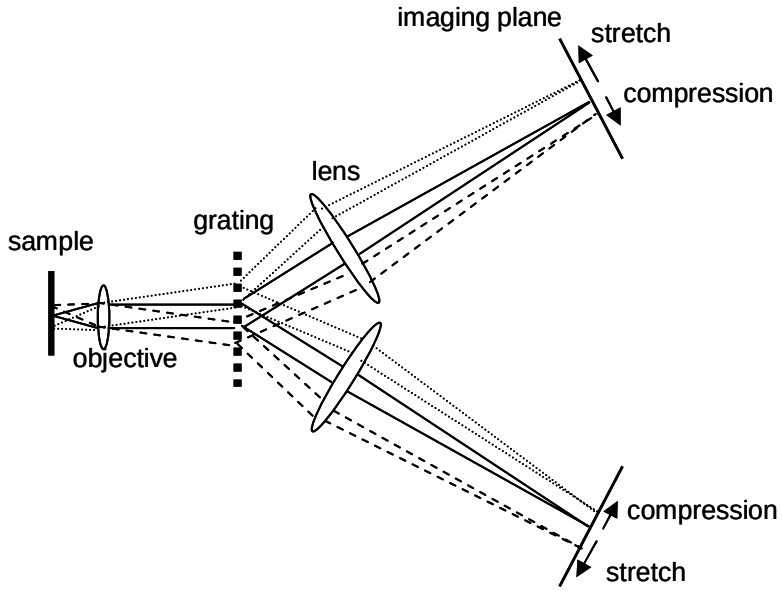

Fig. 4. "Stretch" and "compression" distortion caused by the diffraction of the grating in the imaging system.

4. Improved processing algorithm

In the previous experiment [14], we required the reference power to be much greater than the sample power; this allowed us to neglect the sample power term in the detected signal and simplify image processing. However, this requirement necessarily restricted the dynamic range of our system. By requiring high reference power and low sample power, the ratio of the interference term magnitude to the DC term magnitude was small. This implies that the useful data occupied only a relatively narrow dynamic range of the CCD cameras.

In the current experiment, we removed this restriction and performed imaging processing without simplifying the involved equations. This section details the processing involved.

The detected signal in the corresponding pixels with pixel index (i,j) of the CCDs can be written as

#87235 - $15.00 USD Received 6 Sep 2007; revised 4 Dec 2007; accepted 14 Dec 2007; published 19 Dec 2007

$$P_1(i,j) = P_{r1}(i,j) + P_{s1}(i,j) + A\sqrt{P_{r1}(i,j)P_{s1}(i,j)}\cos(\Delta\psi(i,j)) \tag{11}$$

$$\begin{aligned} P_2(i,j) &= P_{r2}(i,j) + \eta(i,j)P_{s1}(i,j) \\ &\quad + A\sqrt{P_{r2}(i,j)\eta(i,j)P_{s1}(i,j)}\cos(\Delta\psi(i,j) + \Delta\phi) \end{aligned} \tag{12}$$

where $P_{r1}(i, j)$and $P_{r2}(i, j)$are the reference powers at the pixels of CCD1 and CCD2, respectively; $P_{s1}(i, j)$ and $P_{s2}(i, j)$ are the sample powers at corresponding pixels of the CCDs; $\eta(i,j) = P_{s2}(i,j)/P_{s1}(i,j)$ is the relative diffraction efficiency of the grating for the sample beam; A is the interference factor determined by the coherence of the laser, ideally A=2, in practice, the measured A is 1.9; $\Delta\psi(i,j) = \psi_{obj}(i,j) + \psi_{abe}(i,j) + \theta_{ran}$, where $\psi_{obj}(i,j)$ is the optical phase change associated with presence of the sample, $\psi_{abe}(i,j)$ is the phase aberration introduced by the grating as mentioned in the previous section, θ_{ran} is some random phase attributable to environment fluctuation and independent of pixel index (i, j); $\Delta\phi$ is the nontrivial phase shift between the interference signals caused by the G1G2 grating and is independent on the pixel index (i, j).

The experiment procedure for phase extraction can be summarized as follows:

1) Determine the relative diffraction efficiency $\eta(i, j)$.

2) Determine the phase aberration $\psi_{abe}(i,j)$ and the nontrivial phase shift $\Delta\phi$. This involves acquiring N (we use N=100) frame pairs of the interferograms in the absence of the sample. For pixel (i,j) (i=1…1024, j=1…768) of the CCD k (k=1,2), we can get a time series $y_{i,j,k}(n)$, n=1…N. For different n, there is a different random phase introduced by environmental disturbance. Since the time series for any of the two pixels have a phase difference between them, if we plot one time series versus another, we will get an elliptical profile. For the time series from the same CCD, we can let the first pixel (i=1,j=1) be the reference point and compute the phase difference for each CCD pixel with respect to the reference point by performing elliptic fitting [18] between $y_{i,j,k}(n)$ and $y_{1,1,k}(n)$. This computed phase difference is equal to the phase aberration ψ_{abe} . Similarly, by performing elliptic fitting between the corresponding pixels from the two CCDs, $y_{i,j,1}(n)$ and $y_{i,j,2}(n)$, we can get the phase shift $\Delta\phi$.

3) Determine the reference power $P_{r1}(i, j)$ and $P_{r2}(i, j)$.

4) Acquire phase image of the sample. This involves placing the sample into the system and acquiring a frame pair from the two CCDs. The detected signals of corresponding pixels must satisfy Eqs. (11) and (12). The only remaining unknowns are $P_{s1}(i, j)$ and $\Delta\psi(i, j)$.

By canceling $\Delta\psi(i, j)$ from Eqs. (11) and (12), we can obtain a quadratic equation for P_{s1}:

$$\begin{aligned} &\left[\frac{1}{P_{r1}} + \frac{\eta}{P_{r2}} - \frac{2\cos(\Delta\phi)\sqrt{\eta}}{\sqrt{P_{r1}P_{r2}}}\right]P_{s1}^{\,2} - \left[2\frac{P_1 - P_{r1}}{P_{r1}} + 2\frac{P_2 - P_{r2}}{P_{r2}} - \right. \\ &\left. 2\cos(\Delta\phi)\frac{(P_1 - P_{r1})\eta + (P_2 - P_{r2})}{\sqrt{\eta P_{r1}P_{r2}}} + A^2\sin^2(\Delta\phi)\right]P_{s1} \\ &+ \left[\frac{(P_1 - P_{r1})^2}{P_{r1}} + \frac{(P_2 - P_{r2})^2}{P_{r2}\eta} - 2\cos(\Delta\phi)\frac{(P_1 - P_{r1})(P_2 - P_{r2})}{\sqrt{\eta P_{r1}P_{r2}}}\right] = 0 \end{aligned} \tag{13}$$

For clarity, we omitted the functional dependency on (i, j) in the expression. This equation yields two solutions for P_{s1}. In order to find the right solution, the sample power P_{s1} need to

#87235 - $15.00 USD Received 6 Sep 2007; revised 4 Dec 2007; accepted 14 Dec 2007; published 19 Dec 2007

satisfy some condition. As shown in the appendix A, if the real P_{s1} satisfies the following condition, we can always use the smaller solution of Eq. (13) as our solution:

$$\frac{P_{s1}}{P_{r1}}+\frac{P_{s2}}{P_{r2}}-2\sqrt{\frac{P_{s1}}{P_{r1}}\frac{P_{s2}}{P_{r2}}}\cos(\Delta\phi)<\frac{A^2}{4}\sin^2(\Delta\phi) \tag{14}$$

For the ideal quadrature phase shift, $\Delta\phi$=90^o and ideal coherence, A=2, the above condition becomes

$$\frac{P_{s1}}{P_{r1}}+\frac{P_{s2}}{P_{r2}}<1 \tag{15}$$

This condition still requires smaller sample powers compared with the reference powers. However the condition is much less restricted than the requirement of previous system. Having obtained the solution for the sample power P_{s1}, we can then calculate the phase term $\Delta\psi$ by substituting P_{s1} in Eqs. (11) and (12). The phase of the sample plus some uniform random phase is then given by $\psi_{obj}+\theta_{ran}=\Delta\psi-\psi_{abe}$.

The term θ_{ran} tends to be constant over the entire image but it can vary in time. One approach to remove it from a time sequence of phase images is to look at the variation of $\psi_{obj}+\theta_{ran}$ at a location in the image where it is known that ψ_{obj} is not varying. The time dependent variations can then be wholly attributed to θ_{ran}. We can then subtract this value from each image at each time point. This is the approach we employed when we generated phase image movie sequences.

We note that step 1 through 3 need only be done once during calibration.

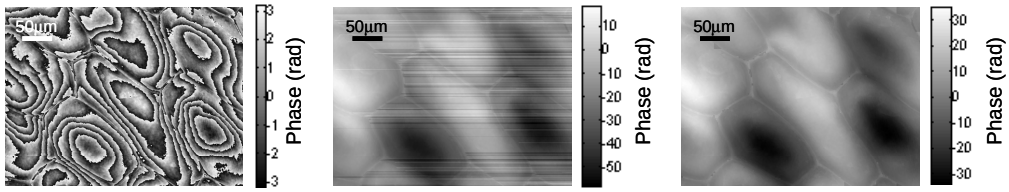

Fig. 5. Compare unwrap algothms. (a) Wrapped image; (b) Unwrapped image by simple unwrap algorithm; (c) Unwrapped image by Flynn's algorithm.

As phase images are intrinsically wrapped beyond the phase range of [0, 2π], we generally need to unwrap the acquired images when dealing with samples beyond a certain thickness. Due to the presence of noise in the phase image, simple unwrap algorithm generally does not work well. For our experiment, we instead chose to use the Flynn's minimum discontinuity algorithm [19] to unwrap the image. Flynn's algorithm operates by identifying the lines of discontinuities and joining them into loops. Appropriate multiples of 2π are then added to each pixel enclosed by the loops to remove the phase wrap discontinuities. This unwrap algorithm worked well for our data. Figure 5 shows an example of the application of unwrap algorithms to our data. Figure 5(a) shows the wrapped phase image acquired by our system. Figure 5(b) shows an unwrapped phase image as generated by the simple unwrap algorithm. Figure 5(c) shows that the Flynn's algorithm is capable of better phase unwrap performance.

To characterize the phase stability of our system, we used a cover glass as our sample and measured the phase difference between two different spots on the cover glass. The phase of the spots is the average of the pixels in the spots with corresponding object size of 1.2 μm x 1.2 μm, matching the diffraction limit of the objective lens. The sample power incident on each spot was 1.6 nW (port 1) and 1.5 nW (port 2). The reference power incident on each spot was 7.6 nW (port 1) and 3.1 nW (port 2). The exposure time per image frame was 100 μs. The

#87235 - $15.00 USD Received 6 Sep 2007; revised 4 Dec 2007; accepted 14 Dec 2007; published 19 Dec 2007

experiment results are shown in Fig. 6. The phase image is shown in Fig. 6(a), and the fluctuation of the phase difference versus time is shown in Fig. 6(b). The phase stability of our system is characterized by the standard deviation of the fluctuation which equals to 62 mrad (corresponding to 6.24 nm optical path length).

We can also estimate the shot noise limited phase noise of our system theoretically, as shown in appendix B. The estimated shot noise limit is 2 mrad, which is much smaller than the experimental measurement. The experimentally measured phase error can be largely attributed to the spatially uncorrelated power fluctuation observed in the experiment. We measured this power fluctuation to be ~3% for each pixel. Substituting this noise factor into our calculation yields a phase noise of ~ 80 mrad, which is comparable to our experimentally measured phase error.

In addition to the phase stability characterization, this set of experiments revealed another aspect of this experimental scheme – we can see some dim fringes in the phase image in Fig. 6(a). These fringes were caused by the relative larger phase noise near some special phase locations. For a simple explanation, consider the quadratic Eq. (13), $aP_{s1}^2+bP_{s1}+c=0$, where a, b, c are the coefficients shown in the equation, the solutions are

$$P_{s1}=\frac{-b\pm\sqrt{\Delta}}{2a},\ where\ \Delta=b^2-4ac \tag{16}$$

The error of the solutions can be written as the function of the measured error of P_1, P_2:

$$\begin{aligned}\delta P_{s1}&=\frac{\partial P_{s1}}{\partial P_1}\delta P_1+\frac{\partial P_{s1}}{\partial P_2}\delta P_2\\&=\frac{-\partial b/\partial P_1\pm(\partial\Delta/\partial P_1)/2\sqrt{\Delta}}{2a}\delta P_1+\frac{-\partial b/\partial P_2\pm(\partial\Delta/\partial P_2)/2\sqrt{\Delta}}{2a}\delta P_2\end{aligned} \tag{17}$$

Thus, when Δ is small, the error of the solution will be large. The fringes in Fig. 6(a) correspond to locations where this effect occurred. Fortunately, in our experiments, this additional phase noise was relatively small (~0.2 rad) and showed up in only a small region of the image.

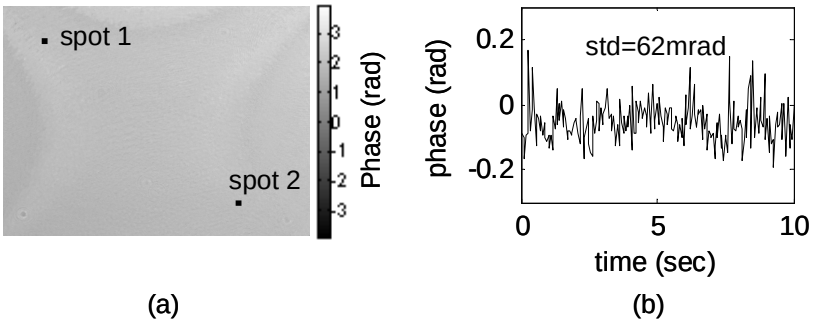

Fig. 6. Measurement of the temporal phase stability. (a) Phase image of a cover glass, the two spots that are used to measure the phase stability are indicated; (b) Fluctuation of the phase of spot 2 with respect to spot 1 versus time, the standard deviation is 62 mrad.

5. Imaging results

As an initial demonstration of our system, we performed phase imaging of a phase object, which consisted of a "CIT" logo written on a 100 nm thick polymethyl methacrylate (PMMA). As expected, the intensity image shown in Fig. 7(a) had little contrast. In comparison, the phase image [Fig. 7(b)] had excellent contrast. Figure 7(c) shows the 3D reconstruction of the phase image. The measured height of a step is shown in Fig. 7(d); the thickness of the logo was measured to be 114±12 nm, which agreed well with the thickness measurement performed with a standard profilometer.

#87235 - $15.00 USD Received 6 Sep 2007; revised 4 Dec 2007; accepted 14 Dec 2007; published 19 Dec 2007

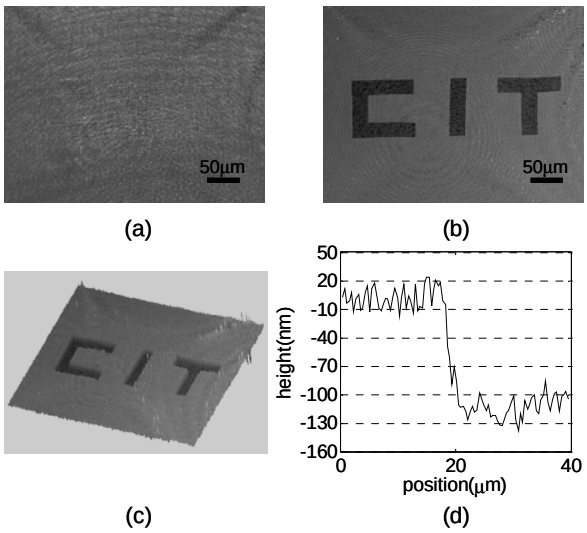

Fig. 7. Images of "CIT" logo by our iamging system. (a) Intensity image; (b) Phase image; (c) 3D reconstruction of the phase image; (d) Step-height measurement.

We next used our system to image onion skin cell (Fig. 8). The intensity and phase images are shown in Figs. 8(a), 8(b), respectively. Figure 8(c) shows the 3D reconstruction of the phase image. Again, the phase image had much better contrast than the intensity image and the optical thickness of the cell can be quantitatively measured from the phase image. The nuclei can be seen clearly in the phase image.

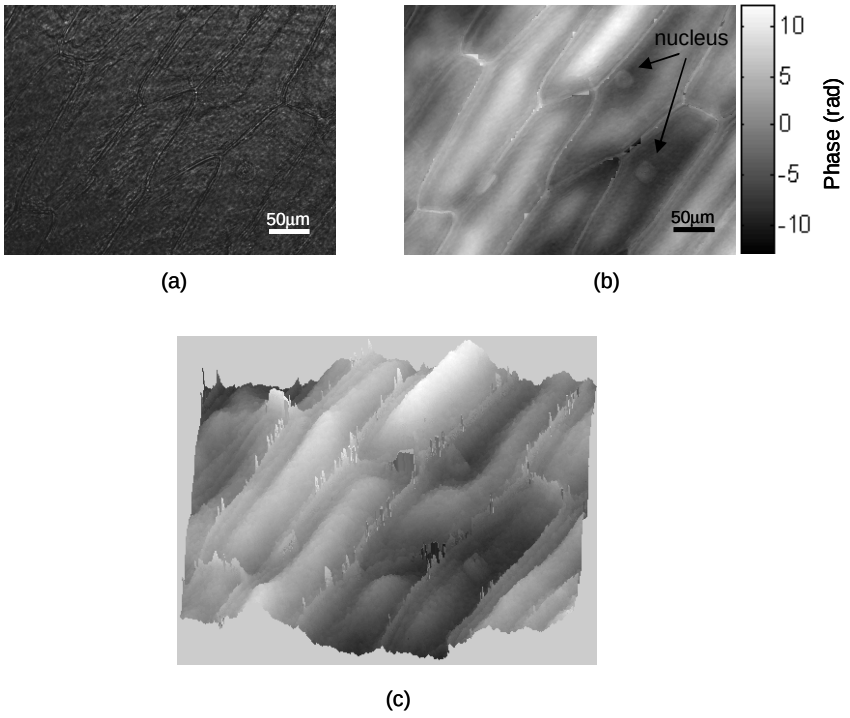

Fig. 8. Images of onion skin cells. (a) Intensity image; (b) Phase image; (c) 3D reconstruction of the phase image.

To demonstrate the capability of our system to study biological movements and dynamics, we applied our system to observe the movement of an amoeba proteus. In the phase movie

#87235 - $15.00 USD Received 6 Sep 2007; revised 4 Dec 2007; accepted 14 Dec 2007; published 19 Dec 2007

[Fig. 9(a)], we can clearly see the nucleus and contractile vacuole of the amoeba. The frame rate of the movie is 10 frames/second. The movement of the food vacuoles can be seen in the movie. Figure 9(b) shows the corresponding intensity movie, which had much poorer contrast.

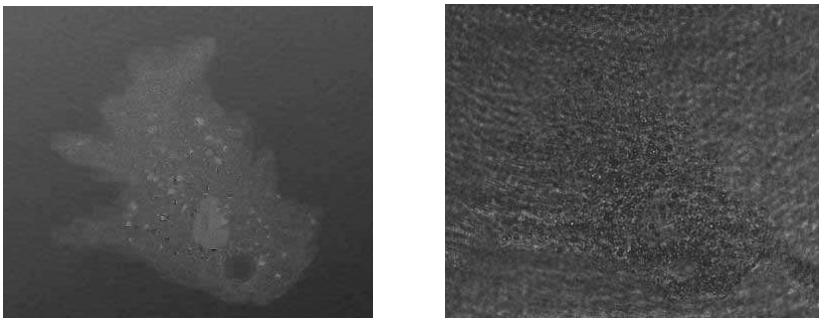

(a) (b)

Fig. 9. (a). (360 KB) MOVIE: phase movie of movement of amoeba proteus. The nucleus and contractile vacuole can be clearly seen. In the movie, the food vacuoles are moving inside the amoeba. The size of one frame is 147 μm (width) x 123 μm (height) (372x312 pixels) (b) (1.66 MB) Movie: intensity movie of movement of amoeba proteus.

6. Summary

We have developed an improved full-field quantitative phase imaging microscope system based on the use of a harmonically matched grating pair (G1G2 grating). This new system design significantly corrected the astigmatic aberration which had restricted the original interferometer design. The system also employed a new phase image processing algorithm which enabled a wide range of sample power to be used in the interferometer.

With these improvements, we were able to demonstrate high resolution phase imaging with a measured resolution of 1.6 μm and a phase sensitivity of 62 mrad (or an equivalent optical path length difference of 6.24 nm). We demonstrate the utility of this interferometer by imaging onion samples and rendering a movie of a moving amoeba proteus.

This phase imaging method is applicable for observing fast dynamics in biological samples as the image acquisition speed is only limited by the frame rate of the cameras. Another appealing aspect of this system is that the heart of the interferometer – the G1G2 grating is a planar device that can be easily designed and fabricated. The feasibility of creating G1G2 grating lithographically or by e-beam etching, also allows for more complicated G1G2 grating designs. For example, it may be interesting to combine Fresnel zone plate and G1G2 grating designs to implement flat phase imaging schemes. In addition, the concept of G1G2 interferometry can be applied to imaging at other wavelengths, such as X-ray or terahertz.

Acknowledgments

This work is supported by NSF career award BES-0547657.

Appendix A: derivation of equation (14)

The derivation for the condition where we can choose one solution out of the two solutions that we get from the quadratic Eq. (13) is as follows. To begin, assume the sample power solution is s_0 and the other solution of Eq. (13) is s_1, then we have

#87235 - $15.00 USD Received 6 Sep 2007; revised 4 Dec 2007; accepted 14 Dec 2007; published 19 Dec 2007

$$s_0 + s_1 = \frac{2\frac{P_1 - P_{r1}}{P_{r1}} + 2\frac{P_2 - P_{r2}}{P_{r2}} - 2\cos(\Delta\phi)\frac{(P_1 - P_{r1})\eta + (P_2 - P_{r2})}{\sqrt{\eta P_{r1} P_{r2}}} + A^2 \sin^2(\Delta\phi)}{\frac{1}{P_{r1}} + \frac{\eta}{P_{r2}} - \frac{2\cos(\Delta\phi)\sqrt{\eta}}{\sqrt{P_{r1} P_{r2}}}} \tag{A.1}$$

If we always have $s_1 > s_0$, then we can choose the smaller solution of the equation and get s_0 that we want. So we should have

$$s_1 > s_0$$

$$\Rightarrow 2s_0 < \frac{2\frac{P_1 - P_{r1}}{P_{r1}} + 2\frac{P_2 - P_{r2}}{P_{r2}} - 2\cos(\Delta\phi)\frac{(P_1 - P_{r1})\eta + (P_2 - P_{r2})}{\sqrt{\eta P_{r1} P_{r2}}} + A^2 \sin^2(\Delta\phi)}{\frac{1}{P_{r1}} + \frac{\eta}{P_{r2}} - \frac{2\cos(\Delta\phi)\sqrt{\eta}}{\sqrt{P_{r1} P_{r2}}}} \tag{A.2}$$

Substitute P_1 and P_2 from Eqs. (11), (12), where $P_{s1} = s_0$, we get

$$\begin{aligned}
&s_0\left(\frac{1}{P_{r1}} + \frac{\eta}{P_{r2}} - \frac{2\cos(\Delta\phi)\sqrt{\eta}}{\sqrt{P_{r1} P_{r2}}}\right) \\
&< \frac{P_1 - P_{r1}}{P_{r1}} + \frac{P_2 - P_{r2}}{P_{r2}} - \cos(\Delta\phi)\frac{(P_1 - P_{r1})\eta + (P_2 - P_{r2})}{\sqrt{\eta P_{r1} P_{r2}}} + \frac{A^2}{2}\sin^2(\Delta\phi) \\
&= \frac{s_0 + A\sqrt{P_{r1} s_0}\cos(\Delta\psi)}{P_{r1}} + \frac{\eta s_0 + A\sqrt{P_{r2}\eta s_0}\cos(\Delta\psi + \Delta\phi)}{P_{r2}} \\
&- \cos\Delta\phi\frac{[s_0 + A\sqrt{P_{r1} s_0}\cos(\Delta\psi)]\eta + [\eta s_0 + A\sqrt{P_{r2}\eta s_0}\cos(\Delta\psi + \Delta\phi)]}{\sqrt{\eta P_{r1} P_{r2}}} + \frac{A^2}{2}\sin^2(\Delta\phi) \\
&\Rightarrow \frac{A\sqrt{s_0}}{\sqrt{P_{r1}}}\sin(\Delta\phi)\sin(\Delta\psi + \Delta\phi) - \frac{A\sqrt{\eta s_0}}{\sqrt{P_{r2}}}\sin\Delta\phi\sin(\Delta\psi) + \frac{A^2}{2}\sin^2(\Delta\phi) > 0
\end{aligned} \tag{A.3}$$

Without loss of generality, we can let $\sin(\Delta\phi) > 0$, thus

$$\begin{aligned}
&\frac{A\sqrt{s_0}}{\sqrt{P_{r1}}}\sin(\Delta\psi + \Delta\phi) - \frac{A\sqrt{\eta s_0}}{\sqrt{P_{r2}}}\sin(\Delta\psi) + \frac{A^2}{2}\sin(\Delta\phi) > 0 \\
&\Rightarrow \left[\frac{A\sqrt{s_0}}{\sqrt{P_{r1}}}\cos(\Delta\phi) - \frac{A\sqrt{\eta s_0}}{\sqrt{P_{r2}}}\right]\sin(\Delta\psi) + \frac{A\sqrt{s_0}}{\sqrt{P_{r1}}}\sin(\Delta\phi)\cos(\Delta\psi) + \frac{A^2}{2}\sin(\Delta\phi) > 0
\end{aligned} \tag{A.4}$$

If for all $\Delta\psi$, the above equation is satisfied, we must have

#87235 - $15.00 USD Received 6 Sep 2007; revised 4 Dec 2007; accepted 14 Dec 2007; published 19 Dec 2007

$$-\sqrt{\left[\frac{A\sqrt{s_0}}{\sqrt{P_{r1}}}\cos(\Delta\phi)-\frac{A\sqrt{\eta s_0}}{\sqrt{P_{r2}}}\right]^2+\left[\frac{A\sqrt{s_0}}{\sqrt{P_{r1}}}\sin(\Delta\phi)\right]^2}+\frac{A^2}{2}\sin(\Delta\phi)>0$$

$$\Rightarrow \frac{P_{s1}}{P_{r1}}+\frac{P_{s2}}{P_{r2}}-2\sqrt{\frac{P_{s1}}{P_{r1}}\frac{P_{s2}}{P_{r2}}}\cos(\Delta\phi)<\frac{A^2}{4}\sin^2(\Delta\phi) \tag{A.5}$$

where $P_{s1} = s_0$ and $P_{s2} = \eta s_0$. This is the Eq. (14).

Appendix B: noise assessment based on system's shot noise

In this appendix we estimate the phase noise associated with the system in the situation where shot noise is the only major noise source. To simplify the problem, we assume that the reference powers and sample powers are the same for the two output ports. We also assume the interference factor A = 2 and the nontrivial phase shift $\Delta\phi = -90^o$. Now the power detected in the two output ports can be written as

$$P_1 = P_r + P_s + 2\sqrt{P_r P_s}\cos\Delta\psi \tag{B.1}$$

$$P_2 = P_r + P_s + 2\sqrt{P_r P_s}\sin\Delta\psi \tag{B.2}$$

So

$$2\sqrt{P_r P_s}\cos\Delta\psi = P_1 - P_r - P_s \tag{B.3}$$

$$2\sqrt{P_r P_s}\sin\Delta\psi = P_2 - P_r - P_s \tag{B.4}$$

We shall assume the detected power P_1 and P_2 contain additive Gaussian white-noise terms x_1, x_2 with zero mean, respectively. For shot noise, the standard deviation of x_1, x_2 should be[20]

$$\sigma_{x_1} = \sqrt{\frac{h\nu}{\eta\tau}P_1}, \quad \sigma_{x_2} = \sqrt{\frac{h\nu}{\eta\tau}P_2} \tag{B.5}$$

where h is the Planck's constant, ν is the light frequency, η is the quantum efficiency of the CCD, and τ is the exposure time. Thus as shown in Fig. B1, the phase noise can be approximately expressed as:

$$\delta\psi \approx \frac{\sqrt{\sigma_{x_1}^2+\sigma_{x_2}^2}}{2\sqrt{P_r P_s}} = \frac{1}{2}\sqrt{\frac{h\nu}{\eta\tau}\frac{P_1+P_2}{P_r P_s}} = \frac{\sqrt{2}}{2}\sqrt{\frac{h\nu}{\eta\tau}\frac{P_r+P_s+\sqrt{P_r P_s}(\cos\Delta\psi+\sin\Delta\psi)}{P_r P_s}}$$
$$\le \frac{\sqrt{2}}{2}\sqrt{\frac{h\nu}{\eta\tau}\frac{P_r+P_s+\sqrt{2P_r P_s}}{P_r P_s}} \tag{B.6}$$

For a typical set of numbers for our system, P_r = 5 nW, P_s = 1.5 nW, η = 0.9, τ = 100 μs, we have $\delta\psi \le 2$ mrad.

We note that the phase noise in shot noise limited detection is more than an order of magnitude smaller than the phase noise (62 mrad) observed in the experiment. This observation indicates that phase noise in our system is dominated by other sources. One probable source is the amount of spatially uncorrelated laser power fluctuations that are observed in our system. We measured the power fluctuation to be approximately equal 3% of

#87235 - $15.00 USD Received 6 Sep 2007; revised 4 Dec 2007; accepted 14 Dec 2007; published 19 Dec 2007

the mean. If we substitute $\sigma_{x_1} = 0.03P_1, \sigma_{x_2} = 0.03P_2$ to model this power fluctuation, we see that the phase noise can be expressed as:

$$\delta\psi \approx \frac{\sqrt{{\sigma_{x_1}}^2 + {\sigma_{x_2}}^2}}{2\sqrt{P_r P_s}} = 0.015\sqrt{\frac{{P^2}_1 + {P_2}^2}{P_r P_s}}$$
$$= 0.015\sqrt{\frac{2(P_r + P_s)^2 + 4P_r P + 4(P_r + P_s)\sqrt{P_r P_s}(\cos\Delta\psi + \sin\Delta\psi)}{P_r P_s}}$$
$$\le 0.015\sqrt{\frac{2(P_r + P_s)^2 + 4P_r P + 4(P_r + P_s)\sqrt{2P_r P_s}}{P_r P_s}} \quad \text{(B.7)}$$

Substituting the typical powers employed in the experiment, we find that $\delta\psi \le 80$ mrad. This corresponds well with the phase error measured in the experiment.

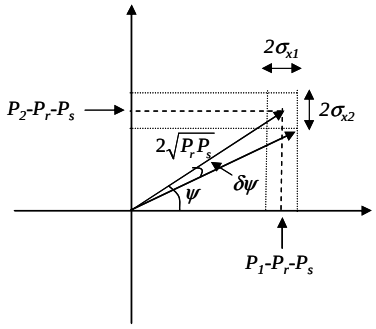

Fig. B1. Schematic of the phase noise assessment.

#87235 - $15.00 USD Received 6 Sep 2007; revised 4 Dec 2007; accepted 14 Dec 2007; published 19 Dec 2007